Small animal imaging with multi-pinhole SPECT

Johan Nuyts
Nuclear Medicine, Katholieke Universiteit Leuven, Belgium
Kathleen Vunckx
Nuclear Medicine, Katholieke Universiteit Leuven, Belgium
Michel Defrise
Nuclear Medicine, Vrije Universiteit Brussel, Belgium
Christian Vanhove
Nuclear Medicine, Vrije Universiteit Brussel, Belgium

correspondence:
Johan Nuyts
Nuclear Medicine, UZ Gasthuisberg
Herestraat 49, B3000 Leuven, Belgium
e-mail: Johan.Nuyts@uz.kuleuven.be
tel: +32 16 34 37 15
fax: +32 16 34 37 59

***Abstract*— With Single Photon Emission Computed Tomography (SPECT), images of minute concentrations of tracer molecules can be acquired, allowing in vivo molecular imaging. For human imaging, the SPECT system has a modest spatial resolution of 5 to 15 mm, a large field of view and a high sensitivity. Using multi-pinhole SPECT, one can trade in field of view for resolution with preserved sensitivity, which enables the implementation of a small animal SPECT system with an improved resolution, currently ranging from 0.3 to 2 mm, in a much smaller field of view. The unconventional collimation and the more stringent resolution requirements pose problems that are not present in clinical SPECT imaging. This paper discusses how these problems can be solved to implement microSPECT imaging on a rotating gamma camera.**

keywords: SPECT, microSPECT, pinhole, tomography, calibration, system matrix, maximum-likelihood, maximum-a-posteriori estimation

I. Introduction

In the last decade, small animal SPECT imaging has made considerable progress, driven by the demands from medical and biological research. Several approaches have been followed to implement small animal SPECT imaging. Some groups converted a clinical gamma camera into a microSPECT system using new collimators and software, others built a whole new system dedicated to high resolution imaging of a small object [1]. Most systems rely on pinhole collimation, although other collimators are being considered, including rotating slit-slat collimators [2], translating slit collimators acquiring linograms [3] and rotating slat collimators [4], [5]. All these collimators scan along converging projection lines resulting in zoomed projections along one or two dimensions, which creates better usage of the available detectors.

This work is supported by F.W.O. grant G.0569.08, by IAP-grant P6/38 and by MOSAIC, the K.U.Leuven Molecular Small Animal Imaging Center (KUL EF/05/08).

In this paper, only multi-pinhole SPECT is considered. Many different system designs have been proposed, ranging from systems based on a rotating gamma camera [6]–[8], a stationary camera with rotating collimator [9] or a completely stationary camera [10]–[12]. We focus on multi-pinhole SPECT using a rotating gamma-camera, although part of what is presented here also holds for stationary systems.

For accurate reconstruction, the projector and backprojector must be based on an accurate model for the system geometry. This can be determined in several ways. The most straightforward one is to scan a small point source through the field-of-view, and directly measure the corresponding point spread function for each of the pinhole apertures [10]–[12]. This approach is slow and requires sophisticated positioning tools, but is highly accurate and directly measures the entire system matrix. It is probably best suited for stationary systems, because they are expected to have a more stable system matrix. In contrast, rotating systems, in particular those based on a clinical gamma camera, have many degrees of freedom and hence can use different system matrices for different scans. For those systems, an easier method to determine the system matrix is useful. In the next section, different approaches for modelling the system matrix are discussed. Finally, an approach to compare the effects of a particular choice of system design parameters on the resolution and noise characteristics of the reconstructed images is discussed.

II. System matrix model

Single or multi pinhole SPECT projections using a rotating gamma camera provide incomplete tomographic information [13]. However, in practice, good reconstructions can be obtained with maximum likelihood (ML) or maximum a posteriori (MAP) reconstruction. The algorithms use a discrete model to represent the unknown tracer distribution and the acquired projections; the relation between the two can be written as

$$Y = AX \quad \text{or} \quad y_i = \sum_j a_{ij} x_j, \tag{1}$$

where Y is a $I \times 1$ matrix containing the measured counts y_i in the detector elements $i = 1 \ldots I$, X is $J \times 1$ matrix with the reconstruction values x_j, and A is the $I \times J$ system matrix. Its element a_{ij} is the expected amount of photons contributed by a unit of activity at position j to the measurement at detector

i. For reconstruction, the elements a_{ij} of the system matrix must be known with good accuracy; system modelling errors will cause reconstruction artifacts.

As discussed above, a first class of methods consists in directly measuring each element of the system matrix [10]–[12]; this *direct method* however requires long acquisitions to collect a sufficient number of counts in each detector i and for each position j of the source. This limitation can be alleviated by measuring the system response for a limited number of positions j of the source that sample the field-of-view; the response for other locations being estimated by interpolation [12]. Fitting a parametric model of the response to the point source measurement can also improve the stability of the estimated system matrix. For non-stationary micro-SPECT systems an additional difficulty with direct methods is the assumption of a perfect reproducibility of the scanner mechanical motion, required to ensure that the calibrated system matrix coincides with the actual matrix at the time of the measurement on the small animal. A potential solution to this problem would be to measure the system matrix A^0 for a single reference position ^{0} of the camera; during reconstruction the image matrix is premultiplied at each position $k = 1, \ldots, K$ of the scanner by a rigid body transformation matrix C^k determined using the geometric calibration described in section II-A. This amounts to writing

$$A = \begin{pmatrix} A^0 C^0 \\ A^0 C^1 \\ \cdots \\ A^0 C^K \end{pmatrix} \tag{2}$$

where K is the number of positions of the camera. Care must be taken to use a robust interpolation when discretizing the geometric transformation to define C^k [14]. A similar decomposition of A has been applied to a micro-PET scanner based on rotating panel detectors [15], though in that case the reference system matrix A^0 was determined by means of a multi-ray method (see below). To our knowledge, this technique has not been applied in micro-SPECT.

A second class of methods estimates the system matrix elements using *Monte-Carlo simulation* [16]–[18]. Starting from an accurate description of all components of the detector, a simulated point source is placed in voxel j of the image matrix, the isotropic emission of a large number N_j of gamma rays is then simulated and the transport of each gamma ray towards the collimator, through the collimator, and finally through the gamma camera is simulated using for instance the Gate software simulation platform. The fraction of the simulated emission that is detected in detector i then yields an estimate $a_{ij} \simeq N_{ij}/N_j$, where N_{ij} is the number of simulated detections in detector i. If the Monte-Carlo simulation perfectly models the system, this method provides a bias-free estimate of a_{ij}, but affected by a relative standard deviation equal to $1/\sqrt{N_j}$. Reducing this standard deviation to an acceptable level while keeping the computation time - even if it is off-line - acceptable is the major challenge of the Monte-Carlo method. The use of variance reduction methods [19] and the ongoing development of a fast version of the Gate software (http://www.fgate.fr/) might in the near future make this approach practical for multiple pinhole SPECT. Note that Monte-Carlo simulation can already now be used to simulate parts of the system matrix, such as the penetration of the gamma rays through the edges of the pinhole aperture. The thus estimated quantities are then used to refine an approximate analytic model of the system matrix [20]. (A similar approach may be based on analytic models of the pinhole aperture [21]–[23]).

Two remarks are in order concerning the two classes of methods discussed so far, direct measurement and Monte-Carlo estimation. First, these methods yield a system matrix that does not model the attenuation and scattering of the gamma rays within the imaged body. This limitation is much less serious for small animal imaging than for clinical imaging, especially for mice. Attenuation correction, when nevertheless deemed necessary, needs to be incorporated separately by premultiplying the image by an attenuation matrix calculated e.g. from a micro-CT scan of the animal. Note that for multiple pinhole collimation, a separate attenuation matrix must be used for each camera position *and* for each pinhole aperture. Scatter correction can be estimated either from a separate, object dependent, Monte-Carlo simulation, or using dual or triple energy windows based methods. A second issue with direct measurement and Monte-Carlo estimation is that these methods are far too time consuming to be applied online. They therefore require storing the measured or calculated system matrix on disk, which is difficult in view of the huge size of the matrix: typically A might be a $10^6 \times 10^6$ matrix. Since object scatter is not included, this matrix is sparse, which reduces the number of non-zero elements to be stored to a more practical level. Additional storage gains may be obtained by considering a single scanner position A^0 as described above, by exploiting symmetries of the scanner, or other compression techniques similar to those proposed by Rehfeld et al [24] for the PET application.

The system matrix measurement time and storage requirements can be further reduced by factorisation. A possible factorisation can be written as

$$A \simeq \sum_{m=1}^{M} A_1^m A_2^m \tag{3}$$

$$A_1^m[i,i] = S_1^m(\vec{i}) \tag{4}$$

$$A_2^m[i,j] = S_2^m(\vec{i}, j, G_D, \theta), \tag{5}$$

where A_1^m are $I \times I$ diagonal matrices and A_2^m are $I \times J$ matrices, $\vec{i} \in I\!R^2$ represents the 2D detector coordinates of element i and G_D is the set of parameters describing the pinhole geometry and θ is the acquisition angle. The summation is over all M apertures of the multi-pinhole system. $S_1^m(\vec{i})$ models the variation of the sensitivity with the angle of the projection line. For a particular aperture m, it depends on the detector position only, and can be measured using a uniform plane source. S_2^m models the blurring due to the aperture and the decrease of sensitivity with increasing distance to the aperture. The computation of S_2^m requires accurate determination of the position of the apertures with respect to the detector and to the object space. A method to determine these parameters is described in the next subsection. The second subsection

briefly discusses the collimator sensitivity measurement, the last subsection presents some resolution modelling approaches.

A. Geometrical calibration

Mathematically, the calibration problem of a pinhole system is identical to that of a cone beam CT [25], [26] or SPECT system [27], [28]. Many authors have studied this problem and a series of different calibration procedures have been proposed. Many of those involve the acquisition of a calibration phantom consisting of point sources [29]–[33]. In these calibration methods, it is assumed that the projection of a point source through an aperture can be described with two coordinates, while in a real image, such a projection shows up as a small blob (fig 1). Typically, the mass center of the blob is computed as an estimate of the intersection of the detector plane and the line defined by the center of the point source and the center of the aperture.

If the gamma camera orbit is perfectly circular with exactly known acquisition angles, the geometry is fully characterised by quantifying the position and orientation of the detector and apertures at the starting angle of the orbit. This involves 6 degrees of freedom (3 translations, 3 rotations) for the detector, plus $3M$ degrees of freedom for the positions of the M apertures. Because the position of the detector along the axis of rotation (z-axis) and the absolute value of the starting angle are arbitrary, 4 + $3M$ degrees of freedom remain. In [31], [34] it was shown that for a single pinhole system, the 7 degrees of freedom can be accurately determined from the SPECT scan of a simple calibration phantom consisting of 3 point sources, provided that at least two of the distances between the point sources are known (as is the detector pixel size). Wang and Tsui [35] proved that for (almost all) multi-pinhole systems, the $4 + 3M$ degrees of freedom can be computed from a SPECT scan of only two point sources, even if the distances between the sources are unknown.

Experience has shown that the orbit of many clinical gamma cameras suffers from small deviations from the ideal circular object. The deviations are sufficiently small to be harmless for human imaging, but were found to adversely affect image quality when the system was used for high resolution imaging with (multi-)pinhole SPECT. Defrise et al [36] modelled these deviations as an independent small rigid motion of the collimator-detector assembly at every projection angle. It was found that a useful estimate of these small motions could be derived from the same SPECT scan of the calibration phantom. In [36], first a calibration was carried out assuming a circular orbit. Then, the refined calibration was treated as a perturbation of this ideal acquisition, which was estimated with singular value decomposition.

In many geometrical calibration methods, it is assumed that for each of the point source projections, the corresponding point source and pinhole aperture have been identified. For a 3 points calibration phantom and a single pinhole aperture, this identification is relatively easy, but for multi-pinhole SPECT it may require tedious manual work or a rather sophisticated algorithm. We found, however, that the identification can be combined within the calibration method as follows. Let

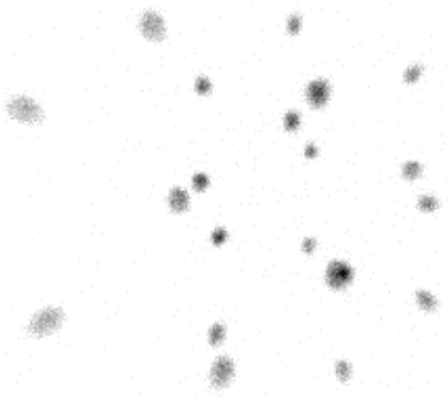

Fig. 1. A projection image of a 3-point calibration phantom, acquired by a 7-pinhole collimator

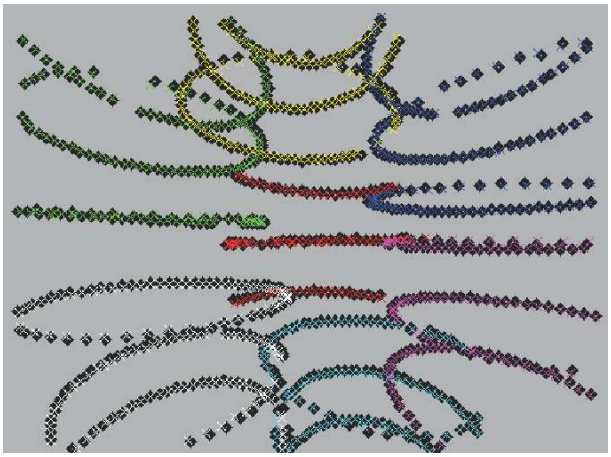

Fig. 2. The calibration result of a 7 pinhole collimator with a 3-point calibration phantom. In black the mass centers of the measured point source projections of all projection angles, and in colour the computed mass centers after refined calibration.

$\vec{u}(\theta, m, p, G_D, G_C)$ be the 2D detector coordinates of the projection of point source p through aperture m for acquisition angle θ, given the geometrical parameters of the detector G_D and the position of the calibration phantom G_C. Although one does not care to know G_C, it has to be determined together with G_D to solve the calibration problem. In our approach, G_C represents 3 translations and 3 rotations, because the calibration phantom is treated as a rigid object with known dimensions. From the SPECT scan of the calibration phantom, one obtains a set of 2D projection images, one for each angle θ. With simple thresholding and mass center computation, this yields a set of 2D coordinates $\vec{u}_k(\theta)$, with $k = 1..K_\theta$ and $K_\theta \leq MP$, where M is the number of apertures and P the number of pinholes. For a particular angle θ, less than MP point source projections may have been found for two reasons: (1) image truncation due to the finite detector size, and (2) identification problems when two point sources projections are so close that the thresholding and/or mass computation failed. It is assumed that such unreliable projections are discarded. To determine the values of the parameters G_D, also the values of m, p, and G_C will have to be determined for each measured projection. This can be done using an iterative least squares

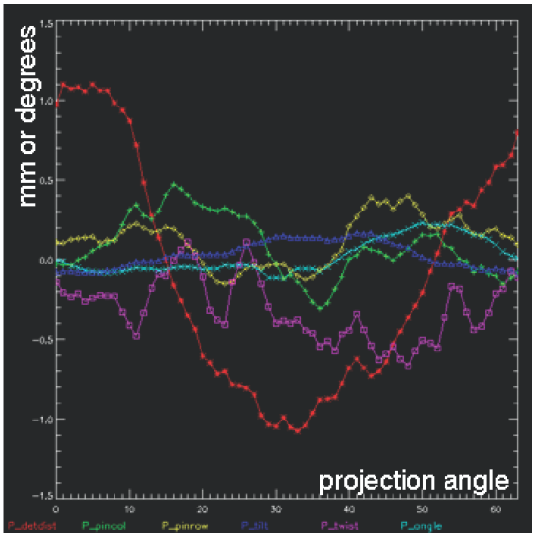

Fig. 3. The rigid camera motions as estimated by the refined calibration procedure. The red curve is a translation towards the rotation axis, green and yellow are the other translations; the other curves represent the rotations.

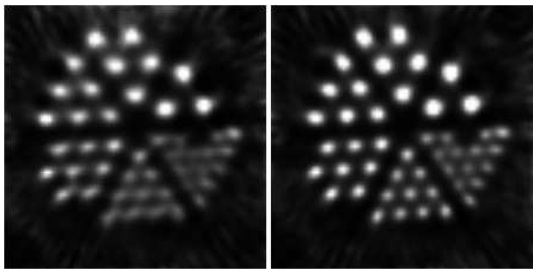

Fig. 4. Reconstruction of a small Jaszczak phantom obtained after calibration assuming an ideal orbit (left) and after refined calibration (right). A 7-pinhole collimator with apertures of 1.5 mm was used, the diameters of the radioactive rods range from 1.5 to 3 mm in steps of 0.3 mm.

algorithm, starting with "reasonable" initial values for G_D and G_C. The algorithm determines G_D and G_C by minimising the distances between each measured point and the closest predicted point:

$$\{\bar{G}_D, \bar{G}_C\} = \underset{G_D, G_C}{\operatorname{argmin}}\, C_1(G_D, G_C) \tag{6}$$

$$C_1(G_D, G_C) = \sum_{\theta,k} \min_{m,p}(|\vec{u}_k(\theta) - \vec{u}(\theta, m, p, G_D, G_C)|^2)$$

This procedure identifies each point projection by assigning it to the aperture m and point source p that minimises the distance between the measured and calculated projection coordinates. Similar to the approach of [36], this initial calibration is refined by finding the angle dependent rigid detector motions that further minimise the residuals:

$$\bar{G}_R = \underset{G_R}{\operatorname{argmin}}\, C_2(\bar{G}_D, \bar{G}_C, \theta, G_R) \tag{7}$$

$$C_2(\bar{G}_D, \bar{G}_C, \theta, G_R) = \sum_k |\vec{u}_k(\theta) - \vec{u}(\theta, m_k, p_k, \bar{G}_D + G_R, \bar{G}_C)|^2 + \sum_{l=1}^{6} \beta_l |G_R[l]|^2 \tag{8}$$

where G_R represents the rigid motion of the detector, and m_k and p_k represent the assignment of the measurement k to the aperture m and point source p, which was determined in the previous step. The last term favours small deviations from the ideal orbit, the weights β_l are tuned empirically. Fig 2 shows a result for a 7-pinhole collimator. Fig 3 shows the small camera motions estimated by the refined calibration. Fig 4 compares the reconstruction with the standard calibration assuming a circular orbit and the reconstruction obtained with subsequent calibration refinement.

In principle, this calibration procedure could also be applied to a stationary multi-pinhole SPECT system, by rotating the calibration phantom inside the field-of-view with small angular increments, acquiring separate projections for each rotation angle.

B. Collimator Sensitivity

If the geometry of the pinhole collimator and the detector is known exactly, the sensitivity S_1^m for each aperture m (see eq (4)) can be estimated analytically or numerically. Schramm et al. [8] used a ray tracing technique to calculate the sensitivity, taking into account the penetration of photons through the collimator, due to the finite attenuation of the collimator material (usually tungsten, although gold [37], [38] and even depleted uranium [39] have been used).

Metzler et al [40] derived an analytical model for knife edge pinholes with axis perpendicular to the detector. In the ideal case of a collimator with infinite attenuation coefficient, the sensitivity to a point source equals [40]:

$$S(\theta, h) = \frac{d^2 \cos^3\theta}{16h^2}, \tag{9}$$

where θ is the angle between the projection line and the normal to the detector, d is the diameter of the aperture and h is the (perpendicular) distance between the point source and the aperture plane. The corresponding sensitivity of detector pixel i to the activity in a plane source equals

$$S_1(i) = \rho \frac{d^2 \cos^3\theta_i}{16f^2} \Delta u \Delta v, \tag{10}$$

where θ_i is the angle defined by i and the aperture position, ρ is the activity per unit area in the plane source, f is the distance between the aperture and the detector, and Δu and Δv are the dimensions of the detector element i. The main difference with (9) is the h-dependence of the latter, which is taken into account by S_2^m in (5). In [40], expression (9) is extended with a term representing the contribution due to penetration of the collimator.

Alternatively, the sensitivity can be measured for each aperture, using a small plane source that can only be seen by a single aperture. Following [8], our collimators consist of a truncated pyramid in lead, to which a tungsten plate with pinhole apertures can be attached. To create a thin plane source, a small vial with flat bottom is filled with a small amount of tracer solution, and put in front of the aperture on the tungsten plate. The advantage of a measurement is that it includes also effects due to energy window settings, crystal penetration, detector non-uniformities, imperfections of

the manufacturing etc.. A disadvantage is that the resulting sensitivity images are corrupted by Poisson noise. The noise can be reduced by fitting an analytical or numerical model, or by applying a low pass or median filter. An example is shown in figure 5.

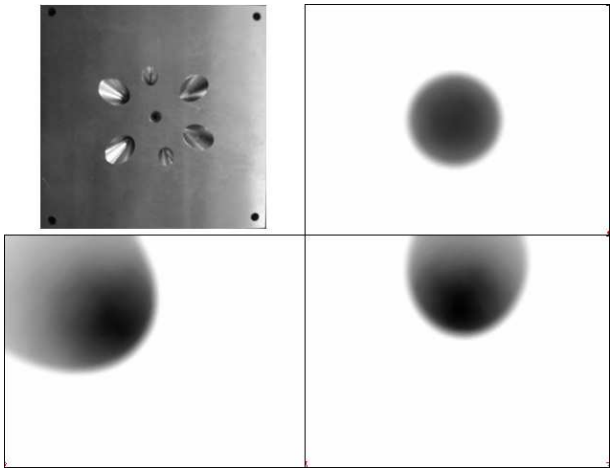

Fig. 5. Backview of a 7-pinhole collimator, and the sensitivity images for the central and two top left apertures.

C. Resolution modelling

The matrix A_2^m in (5) models the effects dependent on j, including the resolution and photon attenuation. In small animals, the effect of attenuation is usually limited, so the impact of A_2^m depends mostly on the resolution model.

Early works in micro-SPECT relied on approximating A_2^m by a simple model A^{geom} which assumes infinitely small ideal pinhole apertures and a perfect spatial resolution of the gamma camera [1]. This idealised model, which is also implicit when using filtered-backprojection algorithms for image reconstruction, is implemented efficiently using ray tracing methods such as Siddon's algorithm. The degradation of image quality caused by using such simple geometric approximations of the system matrix has often been illustrated in PET and in SPECT [41], but the impact is especially dramatic in multi-pinhole micro-SPECT because of the strong non-stationarity of the system response both w.r.t. to the detector location i but also along the line of response, i.e. with respect to the voxel location j. The latter property (*the distance dependant collimator resolution*) refers to the fact that the cone defined by a detector pixel and by one pinhole aperture cannot be reliably approximated by a cylinder because the distance between the animal and the collimator is kept as small as possible to optimise the sensitivity and resolution of the micro-SPECT system. This divergence of the cone prevents approximating the system matrix as a product $A \simeq DA^{geom}$, where D models the detector/collimator resolution, an approach that is appropriate in PET.

We now describe alternative approximate models of the matrix A_2, which are sufficiently simplified to allow online computation, with each element $A_2[i,j]$ being calculated every time it is needed during reconstruction.

[1] A^{geom} depends on m, but m is dropped to simplify the notation

A first solution originally proposed for cone-beam collimators [42] is based on the observation that the shape of the intersection between an image plane parallel to the detector, and the cone defined by a detector pixel and a pinhole aperture is independent of the distance h to the detector, while only the size of this shape increases linearly with the distance h, according to the magnification $\mu = (h+f)/f$ (see figure 6), where f is the focal length of the pinhole. Therefore, if the image matrix is aligned with the detector, resolution modelling can be implemented by convolving each image plane[2], corresponding to a fixed h, with a function $\varphi(x/\mu, y/\mu)$ that models the shape of the cone, scaled by the magnification μ. This convolution is applied prior to applying a simple geometric system matrix A^{geom}, and normally it is applied after rotating the image matrix to align it with the collimator (see matrix C^k in equation 2). A final convolution can be applied after projection (and before backprojection) to model the intrinsic detector resolution.

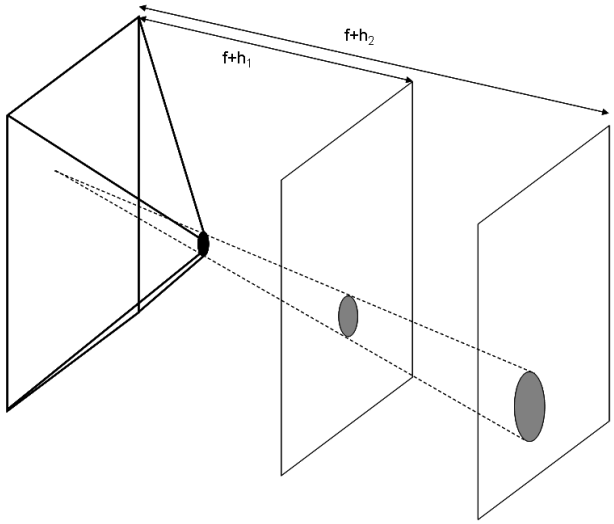

Fig. 6. The blurring effect of the aperture increases linearly as a function of the distance to the aperture.

A second solution, proposed originally for other types of collimators [43], [44], is the *multi-ray approach*: each pinhole aperture is modelled as a set of L ideal, infinitely small apertures $l = 1, \ldots, L$ located to appropriately sample the area of the aperture. The matrix A_2 of (5) is then approximated as

$$A_2 \simeq D \sum_{m=1}^{M} \sum_{l=1}^{L} w_{m,l} A^{geom,m,l} \qquad (11)$$

where $A^{geom,m,l}$ is the system matrix for an ideal pinhole at sub-aperture l of the aperture $m = 1, \ldots, M$; this matrix can be computed efficiently using ray-tracing methods such as Siddon's algorithm. The weights $w_{m,l}$ and the location of the ideal sub-apertures are selected in such a way that the sum in equation (11) yields a good approximation of the exact value represented by an integral over the aperture surface. In [45], [46], for instance, the weights and locations

[2] Unless all apertures are identical, a different convolution kernel φ must be used for each pinhole aperture.

are chosen according to a 2D Gaussian quadrature method with $L = 7$ or $L = 21$ points. The matrix D in equation (11) models the intrinsic detector resolution of the gamma camera, it is typically a convolution with a Gaussian blurring kernel. Compared to the slice by slice blurring method, the multi-ray approach is inefficient numerically, but is easier to generalise[3] and does not require aligning the matrix with the detector. It can also be improved to model the gamma ray penetration of the scintillation crystal by adding sampling points covering the thickness of the scintillator, though this aspect is more important for PET than for micro-SPECT.

To illustrate the impact of accurately modelling the pinhole apertures, we show in figure 7 the ML-EM reconstruction based on an ideal pinhole model, and a multi-ray reconstruction which uses a 7- rays model. Despite the approximate character of the model, there is a significant improvement of image quality. Similar results could be obtained with the other methods described in this section, with potentially further improvements if more accurate models based on direct measurements or Monte-Carlo simulations are used.

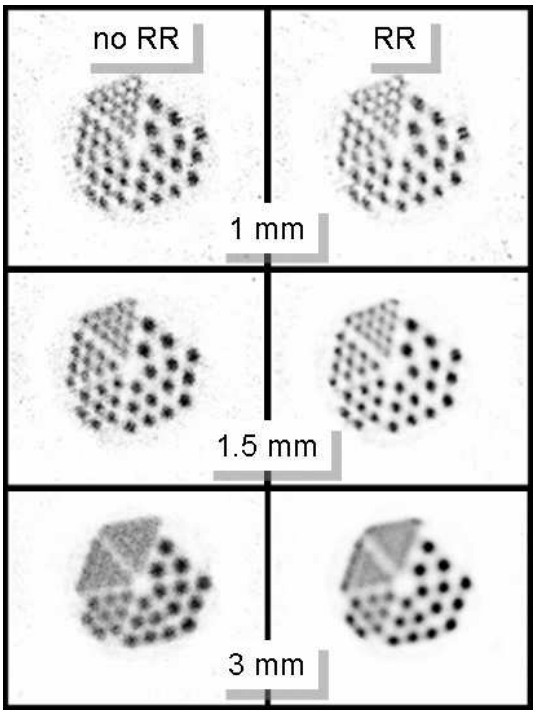

Fig. 7. Reconstruction of a Jaszczak phantom without (left) and with (right) resolution modelling. The diameters of the radioactive rods range from 1.5 to 3 mm in steps of 0.3 mm. Imaging was done with pinhole SPECT using an aperture of 1 mm (top), 1.5 mm (center) and 3 mm (bottom). There were 64 projections, OSEM reconstructions were done with 5 iterations and 16 subsets, the image voxel size was 0.5 mm.

III. Multi-pinhole collimator design

Because of the large amount of parameters (number of apertures, acceptance angles, aperture diameters, positions, distance to the detector etc.), the design of a pinhole collimator is a complex task, which is usually solved empirically. This has led to different strategies. One example is the issue of overlap between projections through different apertures, also called "multiplexing". Some designs avoid all overlap [47], others have extreme multiplexing (e.g. coded aperture [48]), while most designs allow some overlap between the projections (e.g. [8]). Allowing more overlap increases the total amount of measured counts per unit activity in the field-of-view, but at the same time increases the ambiguity of the measured projections, which makes the effect on the quality of the reconstructed images hard to predict.

Assuming that a maximum-likelihood or maximum-a-posteriori reconstruction makes (nearly) optimal use of the data, the resolution and noise characteristics of ML or MAP images could be used to assess the performance of a particular tomographic system for the imaging of a particular object. Barrett et al. proposed a method to calculate the noise propagation as a function of the iteration number for ML-EM reconstructions [49], [50]. However, the computation burden increases with the iteration number. Assuming that MAP is run to convergence, it is possible to compute estimates for the resolution and the covariance from the derivatives of the objective function [51]–[54]. When MAP-reconstruction (or penalised-likelihood reconstruction) is tuned to produce images with shift-invariant resolution, the noise characteristics become very similar to those of a smoothed ML-reconstruction [55], [56]. Consequently, the same approach can be used to predict the noise characteristics of post-smoothed ML or MAP at matched resolution, enabling a relatively straightforward comparison of different tomographic systems for imaging the same object [57], [58]. The systems to be compared are forced to yield images with the same resolution, the system of choice is the one that yields the most favourable noise properties.

This approach is presented in more detail below. The method provides estimates of the resolution and covariance of reconstructed voxel values with good accuracy. However, it provides little information about other relevant image characteristics, such as the possible creation of artifacts due to insufficient sampling. This issue is discussed in the second part of this section.

A. Covariance prediction

1) Theory: To introduce the approach, it is useful to consider the relation between filtered backprojection and unweighted least squares reconstruction, for the case of ideal parallel beam tomography (where the projections are simple unweighted line integrals). The reconstruction problem is given by equation (1), repeated here:

$$Y = AX, \tag{12}$$

where Y is the measurement, A is the system matrix, and X is the activity distribution. Reconstruction involves finding X given Y and A. Least squares reconstruction computes X as follows

$$X_{LS} = \underset{X}{\operatorname{argmin}}(Y - AX)'(Y - AX), \tag{13}$$

where the prime denotes matrix transpose. The solution equals

$$X_{LS} = [A'A]^{-1}A'Y, \tag{14}$$

[3]e.g. to the case of a non planar detector.

provided that the inverse exists. $A'A$ corresponds to the shift invariant blurring obtained by computing the backprojection of the projection of an image. For ideal 2D parallel beam tomography, this blurring is shift-invariant, it is given by the 2D convolution kernel $k(\vec{r}) = 1/|\vec{r}|$. In the frequency domain this corresponds to $1/|\vec{f}|$, where $\vec{f}$ is the frequency. Consequently, the inverse in the frequency domain is $|\vec{f}|$, which is the well-known ramp filter. (Because of the Fourier slice theorem, the order of the filter and backprojection operators can be switched, yielding the filtered backprojection formula.) The matrix $[A'A]$ is very large, and capable of representing a different convolution kernel for every voxel of the image. However, if the blurring is shift invariant, all convolution kernels are the same (or in other words, $[A'A]$ is circulant), enabling application of the much more efficient computations via the Fourier transform.

The reconstruction can be improved by taking into account the noise characteristics of the measurement, e.g. by using a weighted least squares algorithm. In emission tomography, the measured counts are samples from a Poisson distribution, which can be well approximated as a Gaussian distribution. The covariance matrix of the data C_Y is a $I \times I$ diagonal matrix because Poisson noise is uncorrelated. The weighted least squares algorithm computes X as

$$X_{WLS} = \underset{X}{\operatorname{argmin}} (Y - AX)' C_Y^{-1} (Y - AX) \quad (15)$$

$$= [A' C_Y^{-1} A]^{-1} A' C_Y^{-1} Y, \quad (16)$$

where the second equality only holds if the inverse exists. Again, this can be considered as a backproject-then-filter operation, using the weighted backprojection $A'C_Y^{-1}$ and the modified "ramp" filter $[A'C_Y^{-1}A]^{-1}$. Unfortunately, even for a shift invariant tomograph, the matrix $[A'C_Y^{-1}A]$ is not shift invariant, so computing its inverse is intractable for typical SPECT or PET cameras.

However, good approximations can be obtained if one only wishes to compute the impulse response and its covariance in a single voxel j. Consider the true tracer distributions $\bar{X}$ and $\bar{X} + \delta^j$, which only differ by the addition of a small amount of activity to voxel j. The expectations for the corresponding measurements are Y and $Y + A\delta^j$. The expected difference of the corresponding WLS reconstructions equals

$$l^j_{WLS} = [A' C_Y^{-1} A]^{-1} A' C_Y^{-1} A \delta^j \quad (17)$$

$$= \delta^j, \quad (18)$$

which indicates that WLS is an unbiased estimator if the matrix inverse exists. However, in rotating pinhole SPECT, the projections are incomplete, and as a result, the inverse does not exist. Consequently, an approximate inverse G is used, yielding

$$l^j_{WLS} = G A' C_Y^{-1} A \delta^j. \quad (19)$$

Because $A'C_Y^{-1}A$ is a (shift variant) blurring matrix, G is a (shift variant) deblurring operator, usually somewhat similar to the ramp filter. However, because we are only interested in voxel j, because the rest of the image is set to zero and because it is reasonable to assume that the blurring matrix $A'C_Y^{-1}A$ varies slowly with position, Qi et al [53] argued that it is acceptable to ignore the shift invariance. The computations are done for voxel j only, and then applied to all voxels as if the matrices were shift invariant. This can be written as

$$F = A' C_Y^{-1} A \quad (20)$$

$$l^j_{WLS} \simeq G^j F^j \delta^j. \quad (21)$$

The blurring matrix F is also called the Fisher information matrix for estimating X_{WLS} from Y. The matrix F^j is the local approximation of F, obtained by replacing all rows of F with shifted versions of the j-th row of F. Consequently, F^j is a shift invariant blurring operator, coinciding with F for voxel j. G^j is the approximate inverse of F^j, and used as an approximation of G. Finally, the image should be post-smoothed with filter P to suppress the noise and impose the desired spatial resolution. The resulting impulse response is estimated as

$$l^j_{PWLS} \simeq P G^j F^j \delta^j. \quad (22)$$

One usually normalises by setting $\delta^j[j] = 1$. The corresponding covariance matrix can be estimated by propagating the noise covariance through the reconstruction operator. The covariance image C^j_{PWLS} for voxel j is obtained by multiplying the covariance matrix with δ^j. Because we model the reconstruction operator as a shift invariant filter, the computations are tractable:

$$C^j_{PWLS} = PGA' C_Y^{-1} \text{ covar(Y) } C_Y^{-1} A G' P' \delta^j$$

$$= PGA' C_Y^{-1} C_Y C_Y^{-1} A G' P' \delta^j$$

$$= PGFG' P' \delta^j$$

$$\simeq PG^j F^j G^{j'} P' \delta^j$$

Should be P²

$$= P' G^{j'} l^j_{PWLS}. \quad (23)$$

Note that F and G are symmetric matrices, but G^j may be non-symmetric. The last step of (23) is allowed because shift invariant operators commute. C^j_{PWLS} is an image with the same size as the reconstruction image. Its value at voxel k is the covariance of the reconstructed value in k with that in j; hence the value at voxel j is the variance of the reconstruction image in voxel j.

In [57], equations (22) and (23) are obtained by linearisation near the ML or MAP solution, confirming that the same equations can be used to estimate the local (linearised) impulse response and covariance of images reconstructed with ML or MAP algorithms.

In conclusion, with (22) and (23), the impulse response and covariance image for a single voxel can be computed with a projection, a backprojection and a few fast Fourier transforms. Assuming that it suffices to analyse a few tens of voxels to obtain a representative estimate of the image characteristics, the analysis is faster than a single iterative reconstruction, and orders of magnitude faster than a straightforward analysis based on multiple noise realisations.

2) Practice: Application of (22) and (23) to multi-pinhole SPECT can be carried out as described below. It is assumed that a noise-free sinogram Y is given, that a projector and a backprojector implementing A and A' are available, and that software to compute fast Fourier transforms is at hand.

1) Create an image (reconstruction space) which is zero everywhere, then set voxel j to 1. This is δ^j.
2) Compute the (sparse) sinogram $A\delta^j$ by forward multi-pinhole projection of δ^j.
3) Assuming Poisson statistics, the covariance matrix C_Y is a diagonal matrix with elements $C_Y[i,i] = Y[i]$. Consequently, $C_Y^{-1}A\delta^j$ is computed by dividing $A\delta^j$ by Y (element-wise division for each data bin $i = 1 \ldots I$).
4) Compute the image $A'C_Y^{-1}A\delta^j$ by backprojection of the sinogram $C_Y^{-1}A\delta^j$.
5) The image created in the previous step can be regarded as the local point spread function of the modified back-projection near voxel j. The corresponding filter in the frequency domain can be derived by
   a) computing an intermediate image F^j by shifting $A'C_Y^{-1}A\delta^j$ such that j is shifted to the origin (the definition depends on the FFT software), the shift should wrap around the image boundaries.
   b) apply a spatial window function W, which equals 1 at the origin (i.e. near the original value of voxel j) and decreases linearly with distance to the origin. For pinhole SPECT, we used $W(\vec{x}) = (1 - |\vec{x}|/N)$ for an image of $N \times N$ voxels. See below for a note on this window.
   c) compute the Fourier transform $\hat{F}^j$ of F^j, which yields an image with complex valued elements. Zero padding can be used to reduce edge effects.
6) Compute the approximate inverse $\hat{G}^j$ of $\hat{F}^j$, e.g.

$$\hat{G}^j = \frac{\hat{F}^{j*}}{\hat{F}^{j*}\hat{F}^j + \epsilon}, \tag{24}$$

   where * denotes complex conjugate, ϵ is a small positive constant and the multiplication and division are done voxel by voxel. In [57] a slightly different expression was used:

$$\hat{G}^j = \frac{\hat{F}^{j*}\mathcal{R}(\hat{F}^j)_+}{\hat{F}^{j*}\hat{F}^j\mathcal{R}(\hat{F}^j)_+ + \epsilon}, \tag{25}$$

   where $\mathcal{R}$ takes the real part and the subscript $+$ denotes replacing negative values with 0. This modification basically changes the weight of the regularising constant ϵ.
7) Compute $\hat{G}^j * \hat{F}^j$ (where * denotes voxel by voxel multiplication), compute the inverse Fourier transform, and shift the origin back to j. This is the image $G^jA'C_Y^{-1}A\delta^j$. The image is smoothed with the appropriate low pass filter P to yield the image (22). P must be adjusted to ensure that the predefined target resolution is obtained.
8) Compute $\hat{G}^{j*}\hat{G}^j * \hat{F}^j$, compute the inverse Fourier transform, shift the origin back to j to obtain the covariance image of j and post-smooth twice with filter P to obtain the covariance image (23).

A spatial window similar to W was used for fan beam tomography in [54]. We found it to be beneficial in (multi) pinhole SPECT applications as well, but not necessary in more stable tomographic applications, such as time-of-flight PET [59]. The window reduces contributions at large distances from the voxel being studied, which may be beneficial because the true operators have been replaced with a local approximation near voxel j.

3) Applications: This approach was used in [57] to find the best aperture diameter for a particular target resolution. It was found that the diameter should be smaller than the target resolution, such that a noise suppressing low pass filter could be used to obtain the final reconstruction. A similar finding was reported in [60]. In [58], the count rate of a multi-pinhole system was increased by adding pinhole apertures allowing overlap. The SPECT system was used to image a uniform phantom. It was found that image variance initially decreases, but then saturates for a modest amount of apertures: adding more pinholes increases the measured count rate, but apparently the gain is offset by the increased ambiguity. Adding extra shielding to eliminate the overlap increases the performance in center of the field-of-view, at the cost of increased variance near the boundaries of the field-of-view. These studies focussed on the variance of voxel values in the reconstructed image. However, extension to the analysis of the mean and variance of regions-of-interest is straightforward, as was shown in a study of time-of-flight PET [59].

B. Multiplexing artifacts

The method described above accurately predicts the local resolution and noise properties of the reconstruction, but it provides little information on more global image features. With pinhole SPECT using overlapping projections, the creation of multiplexing artifacts has been observed [57], [61], [62]. The problem is illustrated with the cartoon of fig 8. Assume that

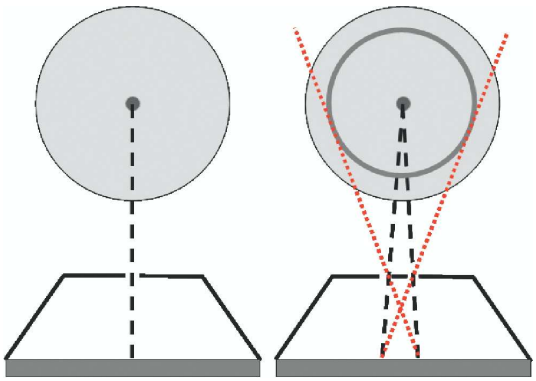

Fig. 8. In multi-pinhole SPECT, the ambiguity creates a "competing" object, its location can be predicted by backprojection through the "wrong" pinhole(s).

a hot point source inside a warm background is scanned with a dual pinhole SPECT system. In every projection image, the point source creates two hot blobs. During reconstruction, the presence of these blobs must be explained as activity along at least some of 4 projection lines. Two of these correspond to the true object, the two others may cause the creation of a "ghost" object. Depending on the amount of ambiguity, this competing ghost object may require a huge amount of iterations to be eliminated. If the ghost object is located on the rotation axis (e.g. when the two pinholes are positioned on a line parallel

to the rotation axis), all "ghost activity" will be accumulated in a small hot spot, which can be very disturbing.

In multi-pinhole SPECT, these ghost objects are more persistent if they are supported by more pinhole apertures. This is illustrated in fig 9 for a simulated two-dimensional 7-pinhole system. Because of the regular pinhole pattern, the ghost objects are supported by multiple pinholes and persist in an OSEM reconstruction after 10 iterations with 18 subsets. By perturbation of the pinhole positions into an irregular configuration, the artifacts are reduced. Also the use of additional information, such as the body outline enclosing the activity, may help to suppress the multiplexing artifacts [63].

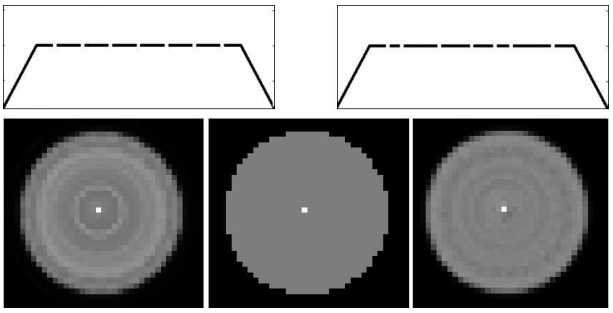

Fig. 9. Comparison of the ML-reconstructions of a regular (left) and an irregular (right) 2D 7-pinhole collimator. The reference image is displayed in the center.

IV. Conclusion

Multi-pinhole collimation enables SPECT imaging of small animals with a useful compromise between sensitivity and resolution. For high quality image reconstruction, the system matrix should be determined accurately. For multipinhole systems that allow overlap between the projections, irregular aperture configurations are recommended to suppress the creation of multiplexing artifacts.

References

[1] SR Meikle, P Kench, M Kassiou, and RB Banati, "Small animal SPECT and its place in the matrix of molecular imaging technologies," *Phys Med Biol*, vol. 50, pp. R45–R61, October 2005.

[2] YP Shao TY Ma, RT Yao, "Determination of geometrical parameters for slit-slat SPECT imaging on microPET," *IEEE Nucl Sci Symp Conf Record*, vol. 1-11, pp. 4285–4288, November 2007.

[3] S Walrand, F Jamar, M de Jong, and S Pauwels, "Evaluation of novel whole-body high-resolution rodent SPECT (linoview) based on direct acquisition of linogram projections," *J Nucl Med*, vol. 46, pp. 1872–1880, November 2005.

[4] Zeng GSL and Gagnon D, "CdZnTe strip detector SPELT imaging with a slit collimator," *Phys Med Biol*, vol. 49, pp. 2257–2271, June 2004.

[5] R. Van Holen, S. Vandenberghe, S. Staelens, and I. Lemahieu, "Comparing planar image quality of rotating slat and parallel hole collimation: influence of system modeling," *Phys Med Biol*, vol. 53, pp. 1989–2002, 3 2008.

[6] RJ Jaszczak, J Li, H Wang, MR Zalutsky, and RE Coleman, "Pinhole collimation for ultra-high-resolution, small-field-of-view spect," *Phys Med Biol*, vol. 39, pp. 425–437, March 1994.

[7] C Vanhove, M Defrise, PR Franken, H Everaert, F Deconinck, and A Bossuyt, "Interest of the ordered subsets expectation maximization (OS-EM) algorithm in pinhole single-photon emission tomography reconstruction: a phantom study," *Eur J Nucl Med*, vol. 27, pp. 140–146, February 2000.

[8] NU Schramm, G Ebel, U Engeland, T Schurrat, M Behe, and TM Behr, "High-resolution spect using multipinhole collimation," *IEEE Trans Nucl Sci*, vol. 50, pp. 315–320, June 2003.

[9] KJ Kearfott and SE Hill, "Simulated annealing image-reconstruction method for a pinhole aperture single photon-emission computed tomograph (SPECT)," *IEEE Trans Med Imaging*, vol. 9, pp. 128–143, June 1990.

[10] RK Rowe, JN Aarsvold, HH Barrett, JC Chen, WP Klein, BA Moore, IW Pang, DD Patton, and TA White, "A stationary hemispherical spect imager for 3-dimensional brain imaging," *J Nucl Med*, vol. 34, pp. 474–480, March 1993.

[11] LR Furenlid, DW Wilson, Y Chen, H Kim, PJ Pietraski, MJ Crawford, and HH Barrett, "FastSPECT II: A second-generation high-resolution dynamic SPECT imager," *IEEE Trans Nucl Sci*, vol. 51, pp. 631–635, June 2004.

[12] F van der Have, B Vastenhouw, M Rentmeester, and FJ Beekman, "System calibration and statistical image reconstruction for ultra-high resolution stationary pinhole SPECT," *IEEE Trans Med Imaging*, vol. 27, pp. 7, 960-971 2008.

[13] HK Tuy, "An inversion formula for cone-beam reconstruction," *SIAM J Appl Math*, vol. 43, pp. 546–552, 1983.

[14] EVR DiBella, AB Barclay, RL Eisner, and RW Schafer, "A comparison of rotation-based methods for iterative reconstruction algorithms," *IEEE Trans Nucl Sci*, vol. 43, pp. 3370–3376, December 1996.

[15] S Moehrs, M Defrise, N Belcari, A Del Guerra, A Bartoli, S Fabbri, and G Zanetti, "Multi-ray-based system matrix generation for 3D PET reconstruction," *Phys Med Biol*, vol. 53, pp. 6925–6945, November 2008.

[16] M Rafecas, B Mosler, M Dietz, M Pogl, A Stamatakis, DP McElroy, and SI Ziegler, "Use of a monte carlo-based probability matrix," *IEEE Trans Nucl Sci*, vol. 51, pp. 2597–2605, May 2004.

[17] D Lazaro, Z El Bitar, V Breton, D Hill, and I Buvat, "Fully 3d monte carlo reconstruction in SPECT," *Phys Med Biol*, vol. 50, pp. 3739–3754, August 2005.

[18] Z El Bitar, Y Petegnief, D Lazaro, D Hill, V Breton, and I Buvat, "Targeted fully 3d monte carlo reconstruction in SPECT," *IEEE Nucl Sci Symp Conf Record*, vol. 6, pp. 3410–3413, 2006.

[19] M Gieles, HWAM de Jong, and FJ Beekman, "Monte Carlo simulations of pinhole imaging accelerated by using kernel forced detection," *Physics in Medicine and Biology*, vol. 47, pp. 1853–1867, June 2002.

[20] C Wietholt, I-T Hsiao, and C-T Chen, "New ray-driven system matrix for small-animal pinhole-SPECT with detector blur, geometric response and edge penetration modeling," *IEEE Nucl Sci Symp Conf Record*, vol. 6, pp. 3414–3419, October 2006.

[21] M Smith and R Jaszczak, "Analytical model of pinhole aperture penetration for 3d SPECT image reconstruction," *Phys Med Biol*, vol. 43, pp. 761–775, 1998.

[22] SD Metzler, JE Bowsher, KL Greer, and RJ Jaszczak, "Analytic determination of the pinhole collimator's point-spread function and rms resolution with penetration," *IEEE Trans Med Imaging*, vol. 21, pp. 878–886, August 2002.

[23] G Bal and PD Acton, "Analytical derivation of the point spread function for pinhole collimators," *Phys Med Biol*, vol. 51, pp. 4923–4950, September 2006.

[24] N Rehfeld and M Alber, "A parallelizable compression scheme for monte carlo scatter system matrices in PET image reconstruction," *Phys Med Biol*, vol. 52, pp. 3421–3437, June 2007.

[25] A Rougée, C Picard, C Ponchut, and Y. Trousset, "Geometrical calibration of x-ray imaging chains for three-dimensional reconstruction," *Comput Med Imaging Graph*, vol. 17, pp. 295–300, 1993.

[26] L von Smekal, M Kachelriess, E Stepina, and W. A. Kalender, "Geometric misalignment and calibration in cone-beam tomography," *Med Phys*, vol. 31, pp. 3242–3266, 2004.

[27] GT Gullberg, BMW Tsui, CR Crawford, JG Ballard, and JT Hagius, "Estimation of geometrical parameters and collimator evaluation for cone beam tomography," *Med Phys*, vol. 17, pp. 264–272, 1990.

[28] P Rizo, P Grangeat, and R Guillemaud, "Geometric calibration method for multiple-head cone-beam SPECT system," *IEEE Trans Nucl Sci*, vol. 41, pp. 2748–2757, 1994.

[29] Y-L Hsieh, GL Zeng, GT Gullberg, and HT Morgan, "A method for estimating the parameters of a fan-beam and cone-beam SPECT system using five point sources," *J Nucl Med*, vol. 34, pp. 191, May 1993.

[30] F Noo, R Clackdoyle, C Mennessier, TA White, and TJ Roney, "Analytic method based on identification of ellipse parameters for scanner calibration in cone-beam tomography," *Phys Med Biol*, vol. 45, pp. 3489–3508, 2000.

[31] D Bequé, J Nuyts, G Bormans, P Suetens, and P Dupont, "Characterization of acquisition geometry of pinhole spect," *IEEE Trans Med Imaging*, vol. 22, pp. 599–612, May 2003.

[32] SD Metzler, RJ Jaszczak, NH Patil, S Vemulapalli, G Akabani, and BB Chin, "Molecular imaging of small animals with a triple-head SPECT system using pinhole collimation," *IEEE Trans Med Imaging*, vol. 24, pp. 853–862, 2005.

[33] FP DiFilippo, MJ Riffe, KM Harsch, NP McCabe, and WD Heston, "Detached multipinhole small animal SPECT device with real-time calibration," *IEEE Trans Nucl Sci*, vol. 53, pp. 2605–2612, October 2006.

[34] D Bequé, J Nuyts, P Suetens, and G Bormans, "Optimization of geometrical calibration in pinhole spect," *IEEE Trans Med Imaging*, vol. 24, pp. 180–190, Februari 2005.

[35] YC Wang and BMW Tsui, "Pinhole SPECT with different data acquisition geometries: Usefulness of unified projection operators in homogeneous coordinates," *IEEE Trans Med Imaging*, vol. 26, pp. 298–308, March 2007.

[36] M Defrise, C Vanhove, and J Nuyts, "Perturbative refinement of the geometric calibration in pinhole SPECT," *IEEE Trans Med Imaging*, vol. 27, pp. 204–214, Februari 2008.

[37] C R Tenney, "Gold pinhole collimators for ultra-high resolution Tc-99m smallvolume," *Conference Record of the IEEE Nucl. Sci. Symp. and Med. Imag. Conf*, vol. 3, pp. 22/44–22/46, 2000.

[38] F van der Have and FJ Beekman, "Photon penetration and scatter in micro-pinhole imaging: a monte carlo investigation," *Phys Med Biol*, vol. 49, pp. 1369–1386, March 2004.

[39] MP Tornai; MF Smith CR Tenney, "Uranium pinhole collimators for positron emission SPECT imaging of small volumes," *IEEE Nuclear Science Symposium Conf Record*, vol. 2, pp. 1038–1042, October 1999.

[40] SD Metzler, JE Bowsher, MF Smith, and RJ Jazczak, "Analytic determination of pinhole collimator sensitivity with penetration," *IEEE Trans Med Imaging*, vol. 20, pp. 730–741, August 2001.

[41] A King, SJ Glick, PH Pretorius, RG Wells, HC Gifford, MV Narayanan, and T Farncombe, "Attenuation, scatter and spatial resolution compensation in SPECT," in *Emission tomography, the fundamentals of PET and SPECT*, MN Wernick and JN Aarsvold, Eds., pp. 473–498. Elsevier Academic, 2004.

[42] GL Zeng, Y-L Hsieh, and GT Gullberg, "A rotating and warping projector-backprojector pair for fan-beam and cone-beam iterative algorithms," *IEEE Trans Nucl Sci*, vol. 41, pp. 2807– 811, 1994.

[43] JK Brown, K Kalki, J Heanue, and BH Hasegawa, "Quantitative spect reconstruction using multiray projection integrators," *IEEE Nucl Sci Symp Conf Record*, vol. 1-3, pp. 1272–1276, October 1995.

[44] GL Zeng, GT Gullberg, BMW Tsui, and JA Terry, "Threedimensional iterative reconstruction algorithms with attenuation and geometric point response correction," *IEEE Trans Nucl Sci*, vol. 38, pp. 693–702, 1991.

[45] C Vanhove A Andreyev, M Defrise, "Pinhole SPECT reconstruction using blobs and resolution recovery," *IEEE Trans Nucl Sci*, vol. 53, pp. 2719–2728, October 2006.

[46] C Vanhove, A Andreyev, M Defrise, J Nuyts, and A Bossuyt, "Resolution recovery in pinhole spect based on multi-ray projections: a phantom study," *Eur J Nucl Med Mol Imaging*, vol. 34, pp. 170–180, February 2007.

[47] FJ Beekman, F van der Have, B Vastenhouw, AJA van der Linden, PP van Rijk, JPH Burbach, and MP Smidth, "A novel system for submillimeter-resolution tomography with radiolabeled molecules in mice," *J Nucl Med*, vol. 46, pp. 1194–1200, July 2005.

[48] SR Meikle, RR Fulton, S Eberl, M Dahlbom, KP Wong, and MJ Fulham, "An investigation of coded aperture imaging for small animal SPECT," *IEEE Trans Nucl Sci*, vol. 48, pp. 816–821, March 2001.

[49] HH Barrett, DW Wilson, and BMW Tsui, "Noise properties of the EM algorithm .1. theory," *Phys Med Biol*, vol. 39, pp. 833–846, May 1994.

[50] DW Wilson, BMW Tsui, and HH Barrett, "Noise properties of the EM algorithm .2. monte-carlo simulations," *Phys Med Biol*, vol. 39, pp. 847–871, May 1994.

[51] JA Fessler, "Mean and variance of implicitly defined biased estimators (such as penalized maximum likelihood): applications to tomography," *IEEE Trans Image Proc*, vol. 5, pp. 493–506, March 1996.

[52] JA Fessler and WL Rogers, "Spatial resolution properties of penalized-likelihood image reconstruction: space-invariant tomographs," *IEEE Trans Image Proc*, vol. 5, pp. 1346–1358, September 1996.

[53] J Qi and RM Leahy, "Resolution and noise properties of MAP reconstruction for fully 3-D PET," *IEEE Trans Med Imaging*, vol. 19, pp. 493–506, May 2000.

[54] YY Zhang-O'Connor and JA Fessler, "Fast predictions of variance images for fan-beam transmission tomography with quadratic regularization," *IEEE Trans Med Imaging*, vol. 26, pp. 335–346, March 2007.

[55] J Nuyts and JA Fessler, "A penalized-likelihood image reconstruction method for emission tomography, compared to postsmoothed maximum-likelihood with matched spatial resolution," *IEEE Trans Med Imaging*, vol. 22, pp. 1042–1052, September 2003.

[56] JW Stayman JA Fessler, "Compensation for nonuniform resolution using penalized-likelihood reconstruction in space-variant imaging systems," *IEEE Trans Med Imaging*, vol. 23, pp. 269–284, March 2004.

[57] K Vunckx, D Bequé, M Defrise, and J Nuyts, "Single and multipinhole collimator design evaluation method for small animal SPECT," *IEEE Trans Med Imaging*, vol. 27, pp. 36–46, January 2008.

[58] K Vunckx, P Suetens, and J Nuyts, "Effect of overlapping projections on reconstruction image quality in multipinhole SPECT," *IEEE Trans Med Imaging*, vol. 27, pp. 972–983, July 2008.

[59] K Vunckx, L Zhou, S Matej, M Defrise, and J Nuyts, "Fisher information-based evaluation of image quality for time-of-flight PET," *IEEE Nuclear Science Symposium Conf Record*, vol. 6, pp. 4129–4136, October 2007.

[60] JA Fessler, "Spatial resolution and noise tradeoffs in pinhole imaging system design: a density estimation approach," *Optics Express*, vol. 2, pp. 237–253, March 1998.

[61] LJ Meng, WL Rogers, NH Clinthorne, and JA Fessler, "Feasibility study of compton scattering enchanced multiple pinhole imager for nuclear medicine," *IEEE Trans Nucl Sci*, vol. 50, pp. 09–16, October 2003.

[62] G Bal, GL Zeng, RM Lewitt, Z Cao, and PD Acton, "Study of different pinhole configurations for small animal tumor imaging," *IEEE Nucl Sci Symp Conf Record*, vol. 5, pp. 3133 – 3137, October 2004.

[63] K Vunckx, J Nuyts, B Vanbilloen, M De Saint-Hubert, D Vanderghinste, D Rattat, FM Mottaghy, and Michel Defrise, "Optimized multipinhole design for mouse imaging," *IEEE Nucl Sci Symp Conf Record*, vol. 7, pp. 4742–4750, November 2008.